Lumped Elastodynamic Model for MEMS: Formulation and Validation

Philippe Cardou, *Student Member, IEEE,* Damiano Pasini, *Member IEEE* and
Jorge Angeles, *Fellow,* ***ASME and*** *IEEE*

Abstract

Proposed in this paper is a symbolic linearly elastodynamic model for the analysis and synthesis of MEMS. In particular, the strain energy in the compliant links is computed from the results of a previous work, by representing beam deflections with small-displacement screws. This allows for a systematic, coherent approach based on screw theory. Two case studies are proposed to illustrate the application of the model. In the first example, the elastodynamic model of a simple accelerometer is derived and compared to one available in the literature. In the second example, a complex accelerometer is modeled, fabricated and tested. Comparison between the simulated results and data from the literature or obtained experimentally shows the accuracy of the proposed model.

Index Terms

Compliant mechanism, accelerometer, dynamics, mechanical systems, stiffness matrix, cross-axis motions, synthesis, analysis.

I. Introduction

The development of micromachining techniques has led to the realization of more sophisticated MEMS devices—see [1, 2]. In most instances, the underlying mechanisms are modeled numerically [3], either through finite element methods [4], or others, such as finite differences [5], relaxation methods [6], or the rigid finite element method [7]. **These methods have been incorporated to numerical synthesis methods, among which we may cite the ground-structure method [8], the load-path synthesis approach [9], and the homogenization method [10]. If these methods apply to a broad range of problems, each solution gives information regarding the single problem that corresponds to the chosen objective function, loads, constraints, mesh, optimization domain, etc. Hence, these numerical methods tend to bury the physics of MEMS under the data. In contrast, when possible, a symbolic approach yields mathematical relations that deepen the insight of the designer. This is thought to be important, especially at the early stage of the design process. Accordingly, the method proposed here may be regarded as a complement to numerical synthesis methods.** The classical approach for the synthesis of compliant micromechanisms is to simplify the representation of the physical problem by making a number of

This work was supported by the *Fonds Québécois de Recherche sur la Nature et les Technologies.*

P. Cardou is with Laval University, Quebec City, QC, Canada.

J. Angeles and D. Pasini are with McGill University, Montreal, QC, Canada.

assumptions, which come at the expense of model accuracy. **As the proposed method targets the early synthesis of MEMS, simplicity of application to a wide range of design variants is thought to be more important than model accuracy, leaving the final dimensional optimization to more accurate numerical methods. Hence, several of the classical assumptions of elastodynamic modeling will be adopted in the formulation below.**

Such assumptions are at the root of other symbolic models for compliant MEMS. One instance of this is the replacement of the compliant links with two or more rigid links articulated with one or more kinematic pairs—generally prismatic or revolute—constrained by translational or torsional springs. This is the idea behind the pseudo-rigid-body model [11]–[13]. The main merit of this method is to be accurate over large displacements while remaining relatively simple, thus allowing for a symbolic approach. However, this method is difficult to implement when it comes to arbitrary displacements in space. Indeed, the pseudo-rigid-body model requires that the spring-driven kinematic pairs be inserted at specific positions on the compliant links of the mechanism. If that link is to deflect about several directions and axes—in translation and rotation—then several kinematic pairs need to be added in series at different positions, which results in a complex kinematics model.

Another common assumption is that of small displacements of the micromechanism rigid-links from their reference poses, which allows the linearization of their dynamics [14]. This assumption is valid in most MEMS applications, since the small displacements involved tend to affect important quantities such as air friction, heat dissipation, and electrostatic forces, but generally have little effect on the inertia and stiffness properties of the mechanism. Hence, the small-displacement assumption will be adopted here.

From the foregoing observations, it would be interesting to have a systematic method for deriving symbolically the complete linearized elastodynamics of complex lumped-compliance micromechanisms undergoing small displacements. To this end, we resort to screw theory. We build upon the work reported in [15], which describes the elastic properties of beams by representing their deformations with small-displacement screws. From these results, we are able to compute the strain energy in a compliant link from the small-displacement screw representing the relative displacement of the two rigid links it connects. The resulting model pertains to the linear theory of elastodynamics [16], and should be relevant to the analysis and synthesis of complex micromechanisms (e.g. [2, 17]).

Two examples are included to illustrate the application of the proposed model. The first example treats the simple case of the ADXL150, an accelerometer produced by Analog Devices; comparison of the results obtained with those reported in [18] is included. The second example addresses the elastodynamics modeling of a complex micromechanism composed of four rigid links and 18 compliant links. The model obtained is compared with experimental results.

II. Dynamic model of Lumped-Compliance Mechanisms Undergoing Small Displacements

Since this is a lumped-parameter model, each component of the flexible mechanism falls into one of two categories. The first category gathers the m *compliant links*, which are assumed to have no inertia and a given non-null compliance in all directions. The second category contains the n *rigid links*, which are attributed a given inertia and no compliance.

Moreover, the compliant links are modeled as Euler-Bernoulli beams, and all the rigid-link displacements are considered to be *small*. From this last assumption, the mass and stiffness properties of the links are assumed to be constant, that is, independent of the mechanism posture.

A. The System Posture

Let us first define the fixed frame $\mathcal{F}$, and frame $\mathcal{R}'_j$ attached to the j^{th} rigid link, as shown in Fig. 1. Moreover, we define frame $\mathcal{R}_j$ as coinciding with frame $\mathcal{R}'_j$ whenever the j^{th} rigid body lies in its equilibrium pose, designated its reference pose. The origins of frames $\mathcal{F}$, $\mathcal{R}_j$, and $\mathcal{R}'_j$ are labeled O, R_j, and R'_j, $j = 1, \ldots, n$, respectively, where R_j is chosen to lie at the mass center of its corresponding rigid link.

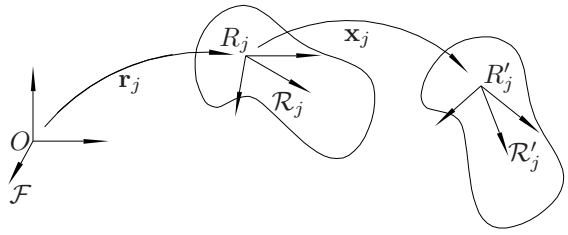

Fig. 1. The j^{th} rigid link in its equilibrium pose and in a displaced pose

The displacement taking $\mathcal{F}$ into $\mathcal{R}_j$ is described by the pose array $\mathbf{r}_j \equiv [\boldsymbol{\theta}_j^T \quad \boldsymbol{\rho}_j^T]^T$, where $\boldsymbol{\theta}_j \in \mathbb{R}^3$ is defined as the product of the natural invariants [19] θ_j and $\mathbf{d}_j$ of the associated rotation and $\boldsymbol{\rho}_j \equiv \overrightarrow{OR_j} \in \mathbb{R}^3$. The natural invariants of a rotation are the unit-vector $\mathbf{d}_j$ pointing in the direction of its associated axis, and its angle of rotation θ_j. In order to avoid ambiguities, we use the right-hand rule in order to determine the direction of the rotation around the screw axis, and we constrain $\boldsymbol{\theta}_j$ within a ball of radius π, that is, $0\,\text{rad} \leq \|\boldsymbol{\theta}_j\|_2 \leq \pi\,\text{rad}$. Notice that this leaves an ambiguity at $\|\boldsymbol{\theta}_j\|_2 = \pi\,\text{rad}$ since, in that case, $\boldsymbol{\theta}_j$ and $-\boldsymbol{\theta}_j$ yield the same rotation. However, since we are using these parameters to describe postures of the mechanism that are close to its static equilibrium posture, this ambiguity may be resolved a priori by the good judgment of the designer.

Similarly, we define the pose of the j^{th} rigid body with respect to its equilibrium pose as

$$\mathbf{x}_j \equiv [\boldsymbol{\nu}_j^T \quad \boldsymbol{\xi}_j^T]^T, \tag{1}$$

where $\boldsymbol{\nu}_j \in \mathbb{R}^3$ is the array of products of the natural invariants for the rotation taking $\mathcal{R}_j$ into $\mathcal{R}'_j$ and following the same convention as that used for $\boldsymbol{\theta}_j$; moreover, $\boldsymbol{\xi}_j \equiv \overrightarrow{R_j R'_j} \in \mathbb{R}^3$. Since the posture of the mechanism is fully described by the poses of all the rigid links, we define the $6n$-dimensional *posture array*

$$\mathbf{x} \equiv \begin{bmatrix} \mathbf{x}_1^T & \mathbf{x}_2^T & \cdots & \mathbf{x}_n^T \end{bmatrix}^T. \tag{2}$$

B. The System Kinetic Energy

For starters, we need an expression for the angular velocity $\boldsymbol{\omega}_j$ of the j^{th} link, which is known to be linear in the derivatives of the linear invariants [19]. We start by computing rather $\boldsymbol{\Omega}_j$, the *angular-velocity* matrix of the j^{th} link, defined as the product $\dot{\mathbf{Q}}_j \mathbf{Q}_j^T$, with $\mathbf{Q}_j$ denoting the rotation matrix that carries $\mathcal{F}$ into an orientation identical to that of $\mathcal{R}_j$, making abstraction of the translation of the origin. In fact, $\boldsymbol{\Omega}_j$ is $\mathrm{CPM}(\boldsymbol{\omega}_j)$, with CPM$(\,\cdot\,)$ denoting the *cross-product matrix*[1] of the three-dimensional Cartesian vector $(\,\cdot\,)$. Once $\boldsymbol{\Omega}_j$ is found, $\boldsymbol{\omega}_j$ is readily derived as its *axial vector*[2], $\mathrm{vect}(\boldsymbol{\Omega}_j)$.

The expression for $\mathbf{Q}_j$ in terms of the linear invariants is recalled for quick reference [19]

$$\mathbf{Q}_j = \mathbf{d}_j \mathbf{d}_j^T + \cos\theta_j (\mathbf{1} - \mathbf{d}_j \mathbf{d}_j^T) + \sin\theta_j \mathrm{CPM}(\mathbf{d}_j),$$

in which $\mathbf{1}$ is the 3×3 identity matrix. Under the "small-displacement" assumption, θ_j is small enough so that $\cos\theta_j \approx 1$ and $\sin\theta_j \approx \theta_j$, the foregoing expression thus reducing to

$$\mathbf{Q}_j \approx \mathbf{1} + \theta_j \mathrm{CPM}(\mathbf{d}_j) \equiv \mathbf{1} + \mathrm{CPM}(\theta_j \mathbf{d}_j) \equiv \mathbf{1} + \mathbf{N}_j \tag{3}$$

where $\mathbf{N}_j \equiv \mathrm{CPM}(\boldsymbol{\nu}_j)$.

Hence, the product $\dot{\mathbf{Q}}_j \mathbf{Q}_j^T$, which yields $\boldsymbol{\Omega}_j$, can be approximated as

$$\boldsymbol{\Omega}_j \approx \dot{\mathbf{N}}_j (\mathbf{1} + \mathbf{N}_j^T) = \dot{\mathbf{N}}_j + \dot{\mathbf{N}}_j \mathbf{N}_j^T \tag{4}$$

The first term of the foregoing expression is *bilinear* in the natural invariants and their time-derivative, the second is *quadratic* in the former, linear in the latter. Under our "small-displacement" assumption, then, we drop the second term and end up with an approximation for $\boldsymbol{\Omega}_j$ involving only the first term of the foregoing expression, whence the approximation of $\boldsymbol{\omega}_j$ follows:

[1]CPM(**a**) is defined as $\partial(\mathbf{a} \times \mathbf{x})/\partial\mathbf{x}$, for any $\mathbf{a}, \mathbf{x} \in \mathbb{R}^3$.

[2]The axial vector $\mathrm{vect}(\mathbf{A})$ of a 3×3 matrix $\mathbf{A}$ is defined, for every three-dimensional vector $\mathbf{x}$, as the three-dimensional vector $\mathbf{a}$ for which $(1/2)(\mathbf{A} + \mathbf{A}^T)\mathbf{x} \equiv \mathrm{CPM}(\mathbf{a})\mathbf{x} \equiv \mathbf{a} \times \mathbf{x}$.

$$\boldsymbol{\omega}_j \approx \dot{\boldsymbol{\nu}}_j, \quad j = 1, \ldots, n. \tag{5}$$

Let us store the mass properties of the j^{th} rigid link into its associated *inertia dyad* [19]

$$\mathbf{M}_j \equiv \begin{bmatrix} \mathbf{I}_j & \mathbf{O} \\ \mathbf{O} & m_j \mathbf{1} \end{bmatrix}, \tag{6}$$

where m_j is the mass of the j^{th} rigid link, $\mathbf{I}_j$ is its inertia matrix about point R_j, its mass centre, and $\mathbf{O}$ is the 3×3 zero-matrix. As a result, the kinetic energy T of the system is computed as

$$T = \frac{1}{2} \sum_{j=1}^{n} \dot{\mathbf{x}}_j^T \mathbf{M}_j \dot{\mathbf{x}}_j = \frac{1}{2} \dot{\mathbf{x}}^T \mathbf{M} \dot{\mathbf{x}}, \tag{7}$$

where

$$\mathbf{M} \equiv \begin{bmatrix} \mathbf{M}_1 & \mathbf{O}_{6\times6} & \cdots & \mathbf{O}_{6\times6} \\ \mathbf{O}_{6\times6} & \mathbf{M}_2 & \cdots & \mathbf{O}_{6\times6} \\ \vdots & \vdots & \ddots & \vdots \\ \mathbf{O}_{6\times6} & \mathbf{O}_{6\times6} & \cdots & \mathbf{M}_n \end{bmatrix}$$

will be referred to as the *mass matrix* of the mechanism.

C. The System Potential Energy

Consider the i^{th} compliant link that is clamped, at one end, to the j^{th} rigid link, and, at the other end, to the k^{th} rigid link, with $j < k$. From the free-body diagram of the i^{th} compliant link shown in Fig. 2(a), we see that the wrench $\mathbf{v}_i \in \mathbb{R}^6$ applied at the mass center R_j by the j^{th} rigid link onto the i^{th} compliant link has to be balanced out by wrench $\mathbf{u}_i(s_i) \in \mathbb{R}^6$ applied at point $S_i(s_i)$, where s_i is a curvilinear coordinate along the beam neutral axis. The wrenches are defined so that their reciprocal product with the small-displacement screws defined in eq. (1) be dimensionally meaningful. Therefore, the first three components of the wrench represent a moment, whereas the last three represent a force, the latter applied at the corresponding mass centre, where the wrench is defined. Let us

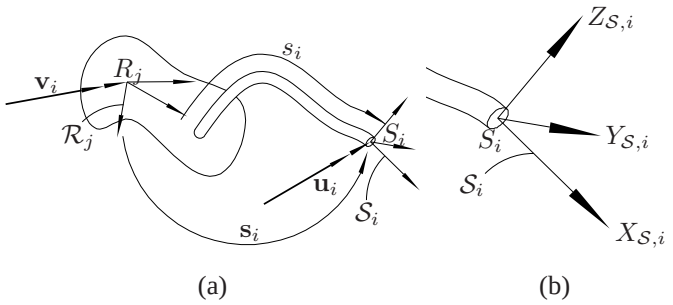

Fig. 2. The i^{th} compliant link attached to the j^{th} rigid link: (a) layout; (b) detail of the definition of $\mathcal{S}_i(s_i)$

attach frame $\mathcal{S}_i(s_i)$ with axes $X_{\mathcal{S},i}$, $Y_{\mathcal{S},i}$, and $Z_{\mathcal{S},i}$, to the beam cross-section at s_i, as shown in Fig. 2(b). Frame $\mathcal{S}_i(s_i)$ is defined so as to have its $X_{\mathcal{S},i}$-axis tangent to the beam neutral axis and pointing in the positive direction

of s_i, and its $Y_{\mathcal{S},i}$- and $Z_{\mathcal{S},i}$-axes along the principal directions of the cross-section. Let $\boldsymbol{\tau}_i(s_i)$ be the array of products of the natural invariants of the rotation taking frame $\mathcal{R}_j$ into frame $\mathcal{S}_i(s_i)$, following the same convention as that used for $\boldsymbol{\theta}_j$, and $\boldsymbol{\sigma}_i(s_i) \in \mathbb{R}^3$ be the vector moving point R_j into $S_i(s_i)$. We regroup these two arrays in the cross-section pose array

$$\mathbf{s}_i(s_i) \equiv [\boldsymbol{\tau}_i(s_i)^T \quad \boldsymbol{\sigma}_i(s_i)^T]^T \in \mathbb{R}^6. \tag{8}$$

Further, let us define $\boldsymbol{\Sigma}_i \equiv \mathrm{CPM}(\boldsymbol{\sigma}_i)$ and $\mathbf{T}_i \equiv \mathrm{CPM}(\boldsymbol{\tau}_i)$.

The strain energy in a beam element of length ds_i starting at coordinate s_i and ending at coordinate $s_i + ds_i$ is computed as [15]

$$dU_i(s_i) = \frac{1}{2}[\mathbf{u}_i(s_i)]^T_{\mathcal{S},i}\mathbf{H}_i(s_i)[\mathbf{u}_i(s_i)]_{\mathcal{S},i}ds_i, \tag{9}$$

where $[\,\cdot\,]_{\mathcal{S},i}$ indicates that the quantity $(\,\cdot\,)$ is expressed in frame $\mathcal{S}_i$ and with respect to its origin S_i. Matrix $\mathbf{H}_i(s_i) \in \mathbb{R}^{6\times 6}$, in turn, contains the properties of the cross-section. This matrix is defined according to the strain energy formulas for beams [20]:

$$\mathbf{H}_i(s_i) \equiv \mathrm{diag}\left(\frac{1}{G_iJ_i}, \frac{1}{E_iI_{Y,i}}, \frac{1}{E_iI_{Z,i}}, \frac{1}{E_iA_i}, \frac{\alpha_{Y,i}}{G_iA_i}, \frac{\alpha_{Z,i}}{G_iA_i}\right), \tag{10}$$

where E and G are the Young and the shear moduli, respectively; $I_{Y,i}$, $I_{Z,i}$ and J_i are the $Y_{\mathcal{S},i}$-axis moment of inertia, the $Z_{\mathcal{S},i}$-axis moment of inertia, and the torsional modulus of the beam cross section, respectively[3]; A_i is the area of the cross-section; and $\alpha_{Y,i}$ and $\alpha_{Z,i}$ are the shearing effect coefficients for the $Y_{\mathcal{S},i}$ and $Z_{\mathcal{S},i}$ directions, respectively. Notice that all these parameters are functions of the curvilinear coordinate s_i.

In the sequel, we shall need the adjoint representation of the Euclidean group [21], which maps linearly the associated Lie algebra onto itself. In the case of the cross-section pose-array screw $\mathbf{s}_i(s_i)$, we obtain

$$\mathbf{S}_i \equiv \begin{bmatrix} e^{\mathbf{T}_i(s_i)} & \mathbf{O}_{3\times 3} \\ \boldsymbol{\Sigma}_i(s_i)e^{\mathbf{T}_i(s_i)} & e^{\mathbf{T}_i(s_i)} \end{bmatrix}, \tag{11}$$

which leads to the following expression of wrench $[\mathbf{v}_i]_{\mathcal{R},j}$ in frame $\mathcal{S}_i$, namely

$$[\mathbf{u}_i(s_i)]_{\mathcal{S},i} = -[\mathbf{v}_i]_{\mathcal{S},i} = -\mathbf{S}_i^T[\mathbf{v}_i]_{\mathcal{R},j}, \tag{12}$$

where the first equality was obtained from the equilibrium in the free-body diagram of Fig. 2(a). Upon substituting eq. (12) into eq. (9) and integrating over the length of the i^{th} compliant link, we obtain the strain energy as

$$U_i = \frac{1}{2}[\mathbf{v}_i]^T_{\mathcal{R},j}\mathbf{B}_i[\mathbf{v}_i]_{\mathcal{R},j}, \tag{13}$$

where

$$\mathbf{B}_i \equiv \int_0^{l_i} \mathbf{S}_i(s_i)\mathbf{H}_i(s_i)\mathbf{S}_i(s_i)^T ds_i,$$

[3] $I_{Y,i}$, $I_{Z,i}$ and J are defined with respect to the centroid of the cross-section.

and l_i is the length of the i^{th} compliant link. It will prove useful to express all wrenches $\mathbf{v}_i$ in the same reference frame $\mathcal{F}$. To do this, we will need the adjoint representation of the Euclidean group that corresponds to the rigid-body motion taking frame $\mathcal{F}$ into frame $\mathcal{R}_j$, namely,

$$\mathbf{R}_j \equiv \begin{bmatrix} e^{\mathbf{\Theta}_i} & \mathbf{O} \\ \mathbf{\Upsilon}_i e^{\mathbf{\Theta}_i} & e^{\mathbf{\Theta}_i} \end{bmatrix}, \tag{14}$$

where $\mathbf{\Theta}_i \equiv \mathrm{CPM}(\boldsymbol{\theta}_i)$ and $\mathbf{\Upsilon}_i \equiv \mathrm{CPM}(\boldsymbol{\rho}_i)$. Hence,

$$[\mathbf{v}_i]_{\mathcal{R},j} = \mathbf{R}_j^T [\mathbf{v}_i]_{\mathcal{F}}, \tag{15}$$

and the total strain energy—or potential energy, for that matter—of the system becomes

$$U = \sum_{i=1}^{m} U_i = \sum_{i=1}^{m} \frac{1}{2} [\mathbf{v}_i]_{\mathcal{F}}^T \mathbf{R}_j \mathbf{B}_i \mathbf{R}_j^T [\mathbf{v}_i]_{\mathcal{F}}. \tag{16}$$

For the sake of conciseness, let us rewrite this expression as

$$U = \frac{1}{2} [\mathbf{v}]_{\mathcal{F}}^T \mathbf{B} [\mathbf{v}]_{\mathcal{F}}, \tag{17}$$

where $\mathbf{B}$ is a block-diagonal matrix, namely,

$$\mathbf{B} \equiv \mathrm{diag}\{\mathbf{R}_{j_1} \mathbf{B}_1 \mathbf{R}_{j_1}^T, \mathbf{R}_{j_2} \mathbf{B}_2 \mathbf{R}_{j_2}^T, \ldots, \mathbf{R}_{j_m} \mathbf{B}_m \mathbf{R}_{j_m}^T\}_{i=1}^m,$$

with j_i taking the value of the smallest index among those of the two rigid links that are connected to the i^{th} compliant link, and

$$[\mathbf{v}]_{\mathcal{F}} \equiv [[\mathbf{v}_1]_{\mathcal{F}}^T \quad [\mathbf{v}_2]_{\mathcal{F}}^T \quad \cdots \quad [\mathbf{v}_m]_{\mathcal{F}}^T]^T.$$

Upon writing the static equilibrium of the wrenches acting on the j^{th} rigid link, we obtain

$$[\mathbf{w}_j]_{\mathcal{R}_j} - \sum_{i \in \mathcal{C}_j^+} [\mathbf{v}_i]_{\mathcal{R}_j} + \sum_{i \in \mathcal{C}_j^-} [\mathbf{v}_i]_{\mathcal{R}_j} = \mathbf{0}_6, \tag{18}$$

where $\mathbf{0}_6$ is the six-dimensional zero-vector, $\mathcal{C}_j^+$ is the set of the indices of the compliant links that are connected to the j^{th} rigid link and to another rigid link that has an index greater than j, while $\mathcal{C}_j^-$ is the set of the indices of the compliant links that are connected to the j^{th} rigid link and to another rigid link that has an index smaller than j. We substitute eq. (15) into eq. (18), and solve for $[\mathbf{w}_j]_{\mathcal{R}_j}$, which leads to

$$[\mathbf{w}_j]_{\mathcal{R}_j} = \mathbf{R}_j^T \left(\sum_{i \in \mathcal{C}_j^+} [\mathbf{v}_i]_{\mathcal{F}} - \sum_{i \in \mathcal{C}_j^-} [\mathbf{v}_i]_{\mathcal{F}} \right). \tag{19}$$

In order to simplify the notation, we define the arrays $\mathbf{v}$ and $\mathbf{w}$ of compliant- and rigid-link wrenches, respectively, that is,

$$[\mathbf{v}]_{\mathcal{F}} \equiv \begin{bmatrix} [\mathbf{v}_1]_{\mathcal{F}} \\ [\mathbf{v}_2]_{\mathcal{F}} \\ \vdots \\ [\mathbf{v}_m]_{\mathcal{F}} \end{bmatrix} \quad \text{and} \quad [\mathbf{w}]_{\mathcal{R}} \equiv \begin{bmatrix} [\mathbf{w}_1]_{\mathcal{R},1} \\ [\mathbf{w}_2]_{\mathcal{R},2} \\ \vdots \\ [\mathbf{w}_n]_{\mathcal{R},n} \end{bmatrix}. \tag{20}$$

Accordingly, we may rewrite eq. (19) in the more convenient form

$$[\mathbf{w}]_{\mathcal{R}} = \mathbf{R}^T \mathbf{A} [\mathbf{v}]_{\mathcal{F}}, \tag{21}$$

where $\mathbf{R} \equiv \mathrm{diag}\{\mathbf{R}_1, \mathbf{R}_2, \ldots, \mathbf{R}_n\} \in \mathbb{R}^{6n \times 6n}$, while

$$\mathbf{A} \equiv \begin{bmatrix} \mathbf{A}_{11} & \mathbf{A}_{12} & \cdots & \mathbf{A}_{1m} \\ \mathbf{A}_{21} & \mathbf{A}_{22} & \cdots & \mathbf{A}_{2m} \\ \vdots & \vdots & \ddots & \vdots \\ \mathbf{A}_{n1} & \mathbf{A}_{n2} & \cdots & \mathbf{A}_{nm} \end{bmatrix} \in \mathbb{R}^{6n \times 6m}. \tag{22}$$

Moreover,

$$\mathbf{A}_{ji} = \begin{cases} \mathbf{O}_{6\times 6} & \text{if compliant link } i \text{ is not connected to rigid link } j; \\ \mathbf{1}_{6\times 6} & \text{if compliant link } i \text{ is connected to rigid links } j \text{ and } k, \text{ with } j < k; \\ -\mathbf{1}_{6\times 6} & \text{if compliant link } i \text{ is connected to rigid links } j \text{ and } k, \text{ with } j > k. \end{cases}$$

This allows the introduction of the *potential energy* of the external wrenches as a function of the internal wrenches, namely,

$$\Pi = -[\mathbf{w}]_{\mathcal{R}}^T [\mathbf{x}]_{\mathcal{R}} = -[\mathbf{v}]_{\mathcal{F}}^T \mathbf{A}^T \mathbf{R} [\mathbf{x}]_{\mathcal{R}}. \tag{23}$$

For a linearly elastic system, the potential energy V and the complementary potential energy $\overline{V}$ take the same value, which is the sum of the strain energy and the potential energy, namely,

$$\overline{V} = V = U + \Pi = (1/2)[\mathbf{v}]_{\mathcal{F}}^T \mathbf{B} [\mathbf{v}]_{\mathcal{F}} - [\mathbf{v}]_{\mathcal{F}}^T \mathbf{A}^T \mathbf{R} [\mathbf{x}]_{\mathcal{R}}. \tag{24}$$

The internal wrenches $\mathbf{v}$ are computed from the minimization of the potential energy V for given displacements $\mathbf{x}$ of the rigid links. This follows from the second theorem of Castigliano. The partial derivative of $\overline{V}$ with respect to the internal wrenches yields

$$\frac{\partial \overline{V}}{\partial [\mathbf{v}]_{\mathcal{F}}} = \mathbf{B} [\mathbf{v}]_{\mathcal{F}} - \mathbf{A}^T \mathbf{R} [\mathbf{x}]_{\mathcal{R}}, \tag{25}$$

whereas the Hessian yields

$$\frac{\partial^2 \overline{V}}{\partial [\mathbf{v}]_{\mathcal{F}}^2} = \mathbf{B}. \tag{26}$$

One may readily verify, from eq. (17), that $\mathbf{B}$ is symmetric, positive-definite and, therefore, all stationary points $\mathbf{v}$ of $\overline{V}$ are minima. Matrix $\mathbf{B}$ being nonsingular, $\partial \overline{V} / \partial [\mathbf{v}]_{\mathcal{F}}$ of eq. (25) admits one single root, namely,

$$[\mathbf{v}]_{\mathcal{F}} = \mathbf{B}^{-1} \mathbf{A}^T \mathbf{R} [\mathbf{x}]_{\mathcal{R}}. \tag{27}$$

Upon substituting eq. (21) into the foregoing equation, we obtain

$$[\mathbf{w}]_{\mathcal{R}} = \mathbf{K} [\mathbf{x}]_{\mathcal{R}}, \quad \text{where} \quad \mathbf{K} \equiv \mathbf{R}^T \mathbf{A} \mathbf{B}^{-1} \mathbf{A}^T \mathbf{R}. \tag{28}$$

The potential energy can now be written as a function of the system posture $\mathbf{x}$, namely,

$$V = (1/2)\mathbf{x}^T\mathbf{K}\mathbf{x}. \tag{29}$$

D. Dissipated Energy

Damping in MEMS is known to be the result of a variety of phenomena (e.g.: air damping, clamp losses, thermoelastic dissipation and crystallographic defects) that are generally nonlinear functions of the system posture x and its derivative $\dot{\mathrm{x}}$. However, for small displacements x and a narrow bandwidth, it is often possible to linearize these funtions around the operating point of the mechanical system. In the case of nonlinear damping, the resulting ordinary differential equation is not likely to admit a closed-form solution. In the analysis that follows, we decided to restrict ourselves to applications where observable damping phenomena may be linearized around the operating point of the system. Moreover, it is assumed that damping acts on the rigid links alone, which allows us to define the Rayleigh dissipation function

$$P = (1/2)\dot{\mathbf{x}}^T\mathbf{C}\dot{\mathbf{x}}, \tag{30}$$

where $\mathbf{C} \in \mathbb{R}^{n\times n}$ is at least positive-semidefinite and contains the system damping coefficients.

E. Dynamic model of the Compliant Mechanism

The Lagrangian of the mechanism is readily computed as

$$L \equiv T - V = (1/2)\dot{\mathbf{x}}^T\mathbf{M}\dot{\mathbf{x}} - (1/2)\mathbf{x}^T\mathbf{K}\mathbf{x}, \tag{31}$$

and its associated Lagrange equations are

$$\frac{d}{dt}\left(\frac{\partial L}{\partial \dot{\mathbf{x}}}\right) - \frac{\partial L}{\partial \mathbf{x}} = -\frac{\partial P}{\partial \dot{\mathbf{x}}} + \mathbf{w} \tag{32}$$

whence,

$$\mathbf{M}\ddot{\mathbf{x}} + \mathbf{K}\mathbf{x} = -\mathbf{C}\dot{\mathbf{x}} + \mathbf{w}, \tag{33}$$

which is the mathematical model sought. As the mass matrix is bound to be symmetric and positive-definite, we can compute its Cholesky decomposition as $\mathbf{M} = \mathbf{L}\mathbf{L}^T$. This allows us to rewrite eq. (33) in its monic representation [22] by performing the change of variable $\mathbf{z} = \mathbf{L}^T\mathbf{x}$, namely,

$$\ddot{\mathbf{z}} + \boldsymbol{\Delta}\dot{\mathbf{z}} + \boldsymbol{\Omega}^{\mathbf{2}}\mathbf{z} = \mathbf{L}^{-\mathbf{1}}\mathbf{w}, \tag{34}$$

where $\boldsymbol{\Delta} \equiv \mathbf{L}^{-1}\mathbf{C}\mathbf{L}^{-T}$ is the *dissipation matrix*, and $\boldsymbol{\Omega}^2 \equiv \mathbf{L}^{-1}\mathbf{K}\mathbf{L}^{-T}$ is the square of the *frequency matrix* of the *undamped* compliant mechanism.

Let μ_i and $\boldsymbol{\mu}_i$, $i = 1, \ldots, n$, be the eigenvalues and eigenvectors of $\boldsymbol{\Omega}^2$, respectively, the former being identical to the natural frequencies-squared, the latter linear transformations of the modal vectors of the undamped system of

eq. (34). That is, if we let λ_i and $\boldsymbol{\lambda}_i$ be the natural frequencies and the modal vectors of the undamped, non-excited system (33), then

$$\begin{aligned} \lambda_i &= \sqrt{\mu_i}, \quad \text{and} \\ \boldsymbol{\lambda}_i &= \mathbf{L}^{-T}\boldsymbol{\mu}_i, \quad i = 1, \ldots, n. \end{aligned} \tag{35}$$

Let us pursue this analysis by computing the Laplace-domain transfer function $\mathbf{H}(s)$, which maps the input wrenches $\mathbf{w}$ acting on the rigid bodies onto the system states $\mathbf{x}$, and where s is the variable of the Laplace domain. From eq. (33), we have

$$\mathbf{H}(s) = \mathbf{L}^{-T}(\mathbf{1}_{6n\times 6n}s^2 + \boldsymbol{\Delta}s + \boldsymbol{\Omega}^2)^{-1}\mathbf{L}^{-1}. \tag{36}$$

In the balance of this article, the proposed mathematical model is applied to two MEMS devices. The ensuing estimates of the dynamic properties are then compared against those obtained from other methods.

III. Analysis of a Simple Case: the ADXL150 Accelerometer from Analog Devices

Even though it is now replaced with the ADXL78, the ADXL150 accelerometer from Analog Devices has been a reference for accelerometer designers [18]. Because of that, its properties are known, and it is thus a good starting point to validate the proposed mathematical model, and to show its usefulness. The ADXL150 has a range of action of $\pm 50g$. It is fabricated using surface-micromachining techniques, which allows for a size as small as $753\,\mu\text{m} \times 657\,\mu\text{m}$, which can be appreciated from Fig. 3. The ADXL150 is a uniaxial accelerometer, and hence, its

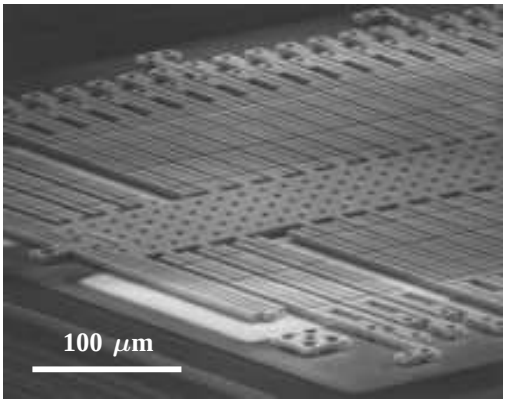

Fig. 3. Analog Devices ADXL150

stiffness should be much lower along its sensitive axis than along any other direction. To verify this, we analyze the mechanical structure of the device, which is sketched in Fig. 4. In this sketch, the thickness t of the compliant mechanism is measured in the **direction orthogonal** to the plane of the figure. The compliant legs are numbered in **encircled numerals** from 1 to 4, whereas the only rigid link of this mechanism is the proof mass itself, which is thus labelled with number 1, in a square. The dimensions are recorded in Table I, as taken from [18], except for b, which was estimated from Fig. 3. Frames $\mathcal{F}$ and $\mathcal{R}_1$ are defined as displayed in Fig. 4, with their X axes along

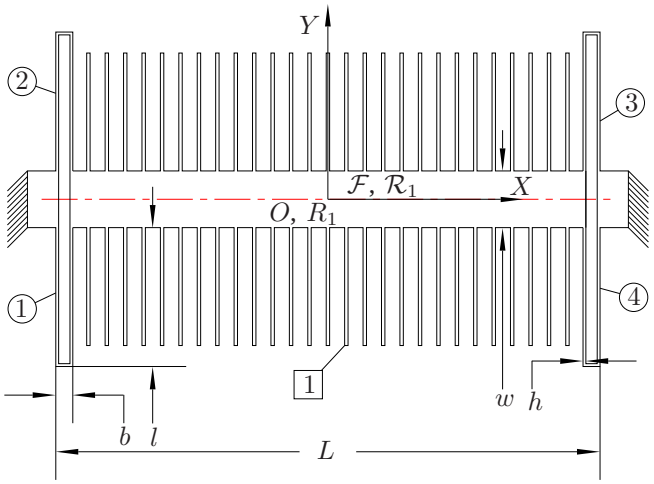

Fig. 4. The mechanical structure of the ADXL150

the accelerometer sensitive axis—represented here by a dashed line, and with their Y axes in the plane of the wafer surface. We take those frames to be right-handed, and so their Z axes stem out of the plane of the wafer surface. Moreover, the origins O and R_1 of these two frames are located at the proof-mass centroid. Hence, apparently, frames $\mathcal{F}$ and $\mathcal{R}_j$ are chosen to be identical, which simplifies subsequent calculations. The material of the flexible

TABLE I
DIMENSIONS OF THE ADXL150 ACCELEROMETER

L	l	w	b	h	t
500 μm	120 μm	50 μm	10 μm	2.5 μm	2 μm

mechanism is polysilicon, which has a Young modulus $E = 160$ GPa, a Poisson ratio $\nu = 0.2$, and a density $\rho = 2331\,\text{kg/m}^3$. The mass matrix $\mathbf{M}$ of the mechanism is the mass matrix of the proof mass as defined in eq. (6). The corresponding inertia matrix **is** estimated to be

$$[\mathbf{I}_1]_{\mathcal{F}} = [\mathbf{I}_1]_{\mathcal{R},1} = \begin{bmatrix} 0.5586 & 0 & 0 \\ 0 & 3.088 & 0 \\ 0 & 0 & 3.647 \end{bmatrix} \times 10^{-18} \quad \text{kg·m}^2 \tag{37}$$

from a CAD model of the proof mass that included its 54 electrodes, **whereas the mass is taken to be** $m_1 = \mathbf{2.2} \times 10^{-10}$ **kg, the same value as that used by [18]**. This allows the evaluation of the kinetic energy from eq. (7).

On the other hand, calculating the potential energy requires the definition of the additional frames $\mathcal{S}_i(s_i)$, $i = 1, 2, 3, 4$. This can be done through the definition of their associated screws $\mathbf{s}_i(s_i)$, $i = 1, 2, 3, 4$, which take frame $\mathcal{R}_1$ into their respective frames $\mathcal{S}_i(s_i)$, $i = 1, 2, 3, 4$. Because the compliant links exhibit discontinuous neutral

axes, these screws are defined as piecewise functions, as detailed in Table II.

TABLE II
SCREWS $\mathbf{s}_i(s_i)$, $i = 1, 2, 3, 4$

$s_i \in$	i	$\mathbf{s}_i^T(s_i)$
[0,l[	1	$\begin{bmatrix} 0 & 0 & 3\pi/2 & -L/2 & -w/2 - s_1 & 0 \end{bmatrix}$
	2	$\begin{bmatrix} 0 & 0 & \pi/2 & -L/2 & w/2 + s_2 & 0 \end{bmatrix}$
	3	$\begin{bmatrix} 0 & 0 & \pi/2 & L/2 & w/2 + s_3 & 0 \end{bmatrix}$
	4	$\begin{bmatrix} 0 & 0 & 3\pi/2 & L/2 & -w/2 - s_4 & 0 \end{bmatrix}$
[l,l+b[	1	$\begin{bmatrix} 0 & 0 & 0 & s_1 - l - L/2 & b - L/2 & 0 \end{bmatrix}$
	2	$\begin{bmatrix} 0 & 0 & 0 & s_2 - l - L/2 & w/2 + l & 0 \end{bmatrix}$
	3	$\begin{bmatrix} 0 & 0 & \pi & L/2 + l - s_3 & w/2 + l & 0 \end{bmatrix}$
	4	$\begin{bmatrix} 0 & 0 & \pi & L/2 + l - s_4 & -w/2 - l & 0 \end{bmatrix}$
[l+b,2l+b]	1	$\begin{bmatrix} 0 & 0 & \pi/2 & b - L/2 & s_1 - 2l - b - w/2 & 0 \end{bmatrix}$
	2	$\begin{bmatrix} 0 & 0 & 3\pi/2 & b - L/2 & 2l + b + w/2 - s_2 & 0 \end{bmatrix}$
	3	$\begin{bmatrix} 0 & 0 & 3\pi/2 & L/2 - b & 2l + b + w/2 - s_3 & 0 \end{bmatrix}$
	4	$\begin{bmatrix} 0 & 0 & \pi/2 & L/2 - b & s_4 - 2l - b - w/2 & 0 \end{bmatrix}$

The beam cross-section remains constant in all the compliant links, and, therefore, from the numerical data of Table II, we obtain,

$$\begin{aligned} J_i &= \beta h t^3 = 3.37 \times 10^{-24}\ \mathrm{m}^4, \quad \text{with} \quad \beta = 0.1685, \\ I_{Y,i} &= t^3 h/12 = 1.67 \times 10^{-24}\ \mathrm{m}^4, \\ I_{Z,i} &= h^3 t/12 = 2.60 \times 10^{-24}\ \mathrm{m}^4, \\ A_i &= ht = 5.00 \times 10^{-12}\ \mathrm{m}^2, \quad \text{and} \\ \alpha_{Y,i} &= \alpha_{Z,i} = 6/5. \end{aligned} \tag{38}$$

Since frames $\mathcal{F}$ and $\mathcal{R}_1$ are coincident, we have

$$\mathbf{R} = \mathbf{R}_1 = \mathbf{1}_{6\times 6}, \tag{39}$$

and, because the four compliant links connect the fixed rigid link to the only mobile rigid link, we may assign

$$\mathbf{A} = \begin{bmatrix} -\mathbf{1}_{6\times 6} & -\mathbf{1}_{6\times 6} & -\mathbf{1}_{6\times 6} & -\mathbf{1}_{6\times 6} \end{bmatrix}, \tag{40}$$

where the minus sign comes from the assumption that the fixed rigid link corresponds to the index $j = 0$. From eq. (28), we obtain directly

$$\begin{aligned} \mathbf{K} = \mathrm{diag}\big(&2.87 \times 10^{-8},\ 1.94 \times 10^{-7}, \\ &1.61 \times 10^{-5},\ 5.16,\ 268,\ 3.17\big), \end{aligned} \tag{41}$$

whose first three entries bear units of N·m/rad, the last three of N/m. The fourth diagonal term in eq. (41) represents the stiffness of the mechanism along the accelerometer sensitive axis. The value reported in [13] for the same

TABLE III
MODAL ANALYSIS OF THE ADXL150 ACCELEROMETER

i	1	2	3	4	5	6
f_i (kHz)	19.11	24.38	36.08	39.90	175.60	334.62
$\boldsymbol{\lambda}_i$	0.000	0.000	1.000	0.000	0.000	0.000
	0.000	0.000	0.000	1.000	0.000	0.000
	0.000	0.000	0.000	0.000	0.000	1.000
	0.000	1.000	0.000	0.000	0.000	0.000
	0.000	0.000	0.000	0.000	1.000	0.000
	1.000	0.000	0.000	0.000	0.000	0.000

dimensions was 5.6 N/m, but this did neither take into account the deflection of the shorter intermediate straight beams in each leg, **i.e., the beams with a length of** $b = 10$ μ**m,** nor the shear strain in any of the beams. According to [18], the actual value measured by Analog Devices is 5.4 N/m. **Hence, in this case study, the proposed model appears to be accurate.**

The frequency matrix can thus be computed from its definition, in eq. (34), which yields

$$\begin{aligned} \boldsymbol{\Omega} &= \operatorname{diag}(2.27 \;\; 2.51 \;\; 21.0 \;\; 1.67 \;\; 12.0 \;\; 1.31) \times 10^5 \text{ rad/s}, \\ &= \operatorname{diag}(36.1 \quad 39.9 \quad 335 \quad \mathbf{24.4} \quad \mathbf{176} \quad \mathbf{19.1}) \quad \text{kHz}. \end{aligned}$$

Apparently, the frequency matrix is diagonal, which allows for the extraction of its eigenvalues and eigenvectors by simple inspection. For the sake of clarity, these values are listed in Table III, in ascending order.

A natural frequency of 24.7 kHz is reported in [18] in the direction of the accelerometer sensitive axis, which is somewhat **larger** than the $\mathbf{24.4}$ kHz obtained here. The reason behind **this** is the different stiffness **estimate, which, in the case of [18], did not take into account the shear strain nor the compliance of the intermediate beam in each leg of the ADXL150**. There is a relatively large difference between the fundamental frequency and that of the mode in the direction of the accelerometer sensitive axis, as compared to the small difference of the former with that of a translational out-of-plane motion of the proof mass, which may surprise anyone who is not familiar with MEMS design. Indeed, at this scale, the damping due to the squeezed film of air between the proof mass and the substrate is extremely high in that direction, which prevents this parasitic motion from becoming significant at high frequencies.

To substantiate this claim, let us estimate the damping in the system by assigning some values to matrix $\mathbf{C}$ defined in eq. (30). Here, we consider only the damping that is due to air friction beneath the proof mass and between the electrodes. Moreover, even though it may be just as high as the damping due to proof-mass translations, we neglect air damping due to **proof-mass** rotations. This choice is mainly justified by virtue of correspondence of the lowest frequencies of the system to those of the translational proof-mass motions; the choice can also be justified by the

level of complexity associated with the modeling of the air flow around a rotating plate close to a flat surface. Indeed, the air flow beneath the proof mass induced by in-wafer-plane translations may be modeled as a simple Couette[4] flow, whereas the air flow produced by out-of-wafer-plane translations may be assimilated to a Poiseuille[5] flow [18]. Moreover, as a rough approximation, we consider the flow between the electrodes as well as when the proof mass translates in the X-axis direction to be of the Poiseuille type; we consider a Couette flow when the proof mass translates in the Y-axis direction. As a result, we have

$$\begin{aligned}\mathbf{C} \;=\; \mathrm{diag}\{0,\, 0,\, 0,\, &\eta(L-2b)w/c + 108\times 96\eta l t^3/(\pi^4 d^3),\\ &\eta(L-2b)w/c + 108\eta l t/d,\\ &96\eta(L-2b)w^3/(\pi^4 c^3)\},\end{aligned} \tag{42}$$

i.e.,

$$\begin{aligned}\mathbf{C} \;=\; \mathrm{diag}\{0,\, 0,\, 0,\, &1.107\times 10^{-6},\\ &0.629\times 10^{-6},\, 259.858\times 10^{-6}\}\ \mathrm{N\,s/m},\end{aligned} \tag{43}$$

where $c = 1.6\,\mu$m is the gap between the proof mass and the chip, $d = 1.3\,\mu$m is the gap between two electrodes, and $\eta = 18\times 10^{-6}$ Pa s is the dynamic viscosity of air.

The associated matrix transfer function is computed from eq. (36). In the case of an accelerometer, the array of rigid-link external wrenches $\mathbf{w}$ defined in eq. (20) may be regarded, from d'Alembert's principle, as an array of *inertial wrenches*. Moreover, if we assume that the instant screw axis of any motion of the accelerometer frame lies at infinity, which is reasonable for a small mechanical system, we can neglect the angular velocity and write $\mathbf{w}$ as a linear function of the twist time-derivative $\mathbf{a}$ of the accelerometer frame. Hence, the acceleration field of the accelerometer frame is approximated by a helical field represented by screw $\mathbf{a}$, which is formed with the angular acceleration of frame $\mathcal{F}$ with respect to an inertial frame, and the acceleration of its origin O with respect to a fixed reference point, both expressed in the accelerated frame $\mathcal{F}$. Symbolically, we obtain

$$\mathbf{w} = -\mathbf{M}\mathbf{R}^T\mathbf{T}\mathbf{a}, \tag{44}$$

where $\mathbf{T} \equiv [\mathbf{1}_{6\times 6} \quad \mathbf{1}_{6\times 6} \quad \cdots \quad \mathbf{1}_{6\times 6}]^T$.

Let us now label ξ_X, ξ_Y, and ξ_Z the components of the position of the proof-mass position vector $\boldsymbol{\xi}_1$, and a_X, a_Y, and a_Z the components of $\mathbf{a}$. We also define unit vectors $\mathbf{e}_4 \equiv [\mathbf{0}_3^T \quad 1 \quad \mathbf{0}_2^T]^T$, $\mathbf{e}_5 \equiv [\mathbf{0}_4^T \quad 1 \quad 0]^T$, and

[4]A Couette flow is a laminar flow of an incompressible Newtonian fluid induced by the relative motion of the two parallel planes in relative translation that contain the fluid [23].

[5]A Poiseuille flow is a laminar flow of an incompressible Newtonian fluid in a pipe [23].

$\mathbf{e}_6 \equiv [\mathbf{0}_5^T \quad 1]^T$, which lets us write the input-output relationships

$$h_X(s) \equiv \xi_X(s)/a_X(s) = -\mathbf{e}_4^T \mathbf{H}(s)\mathbf{M}\mathbf{R}^T\mathbf{T}\mathbf{e}_4, \tag{45}$$

$$h_Y(s) \equiv \xi_Y(s)/a_Y(s) = -\mathbf{e}_5^T \mathbf{H}(s)\mathbf{M}\mathbf{R}^T\mathbf{T}\mathbf{e}_5, \tag{46}$$

$$h_Z(s) \equiv \xi_Z(s)/a_Z(s) = -\mathbf{e}_6^T \mathbf{H}(s)\mathbf{M}\mathbf{R}^T\mathbf{T}\mathbf{e}_6. \tag{47}$$

We compute the complex frequency responses $h_X(\omega)$, $h_Y(\omega)$, and $h_Z(\omega)$ of the proof mass to transverse accelerations by evaluating the corresponding transfer functions at $\omega\sqrt{-1}$, where ω is the input frequency. Upon computing the magnitudes and phase angles of these complex functions, we obtain the Bode plots of Fig. 5.

From the magnitude-vs.-frequency plot of Fig. 5(a), we see that the accelerometer response to Z-axis accelerations is overdamped, whereas the responses to in-wafer plane accelerations are underdamped. Nevertheless, the out-of-wafer-plane motion can still pose problems when the proof mass is subjected to low-frequency accelerations (e.g. gravitational or centripetal) along the Z-direction of frame $\mathcal{F}$. Indeed, cross-axis sensitivity is the highest source of errors ($\pm 2\%$ of the full-scale range, i.e., $1g$) for the ADXL150 accelerometer.

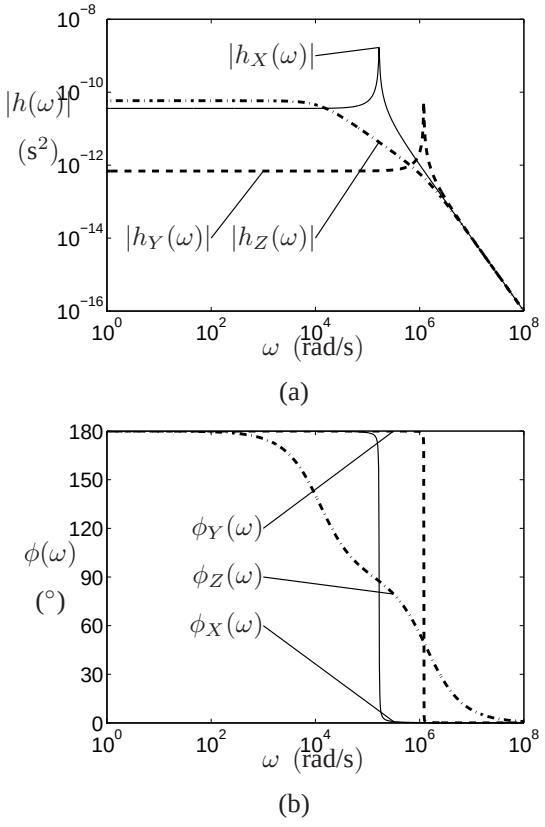

Fig. 5. Frequency response of the ADXL150: (a) magnitude and (b) phase

IV. Analysis of a Complex Case: the Simplicial Biaxial Accelerometer

Let us now turn our attention towards a more complex mechanical architecture, that of the *Simplicial Biaxial Accelerometer* (SBA) [24], which is shown in Fig. 6. The proof mass of this accelerometer takes the shape of a regular triangle. This triangle is suspended at each of its edges by a pair of *distal* beams, which connects at its other ends to an intermediate rigid link. In turn, this rigid link is suspended by four *proximal* beams perpendicular to their corresponding pair of distal beams, which connect to the accelerometer frame at their other ends. As a result, this mechanism is compliant to proof-mass translations in the wafer plane, while offering high stiffness to proof-mass rotations and translations out of the wafer plane. **The equilateral triangular geometry of the SBA resembles that of the HexFlex [25] while resulting in a completely different mechanical behavior. If the SBA allows for in-plane translations of its moving platform, the HexFlex allows for any displacements of its moving platform in space. Moreover, in the case of the SBA, the moving platform serves as an acceleration sensor, whereas the HexFlex moving platform is actuated through its supporting legs.** A prototype of the **packaged microfabricated** device is shown in Fig. 7.

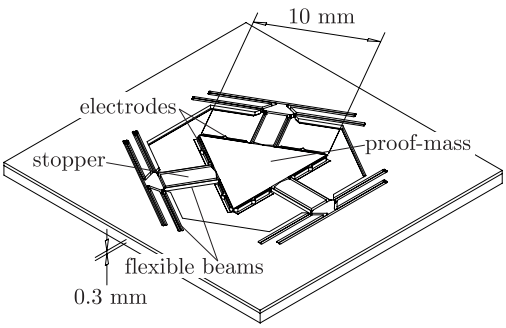

Fig. 6. CAD model of the *Simplicial Biaxial Accelerometer* (SBA)

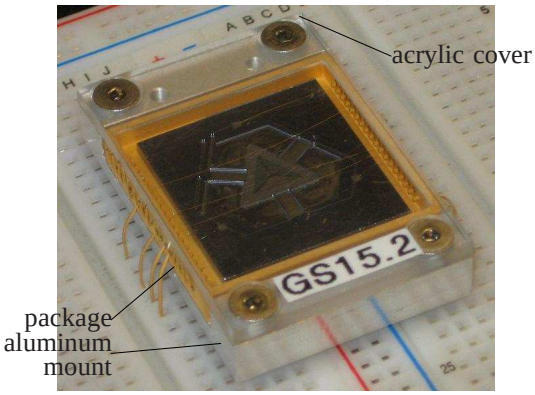

Fig. 7. Packaged microfabricated SBA

For the purpose of this analysis, a top view of the SBA is shown in Fig. 8, where each link is labelled with a number appearing in a circle for a compliant link, and in a box for a rigid link. Table IV lists the numerical values of the dimensions appearing in Fig. 8 as well as the numerical value of the device wafer thickness t.

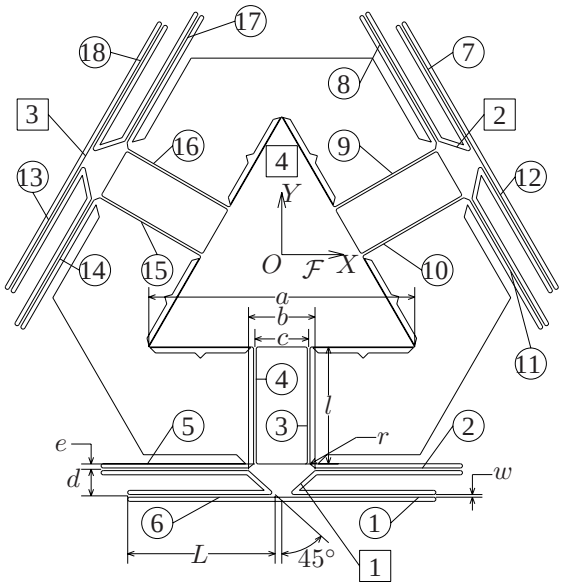

Fig. 8. Dimensions of the *Simplicial Biaxial Accelerometer*

TABLE IV
DIMENSIONS OF THE SIMPLICIAL BIAXIAL ACCELEROMETER

L	l	w	t	r
5544 μm	4400 μm	105 μm	300 μm	78.7 μm
a	b	c	d	e
10000 μm	2500 μm	2020 μm	1000 μm	200 μm

A. Kinetic Energy

Frames $\mathcal{R}_j$, $j = 1, \ldots, n$, $n = 4$, are located at the mass centers of their corresponding rigid links, and oriented so that screws $\mathbf{r}_j$, $j = 1, \ldots, n$, take the values

$$\begin{aligned}
\mathbf{r}_1 &= \begin{bmatrix}\mathbf{0}_4^T & -\sqrt{3}a/6 - l - f & 0\end{bmatrix}^T, \\
\mathbf{r}_2 &= [\mathbf{0}_2^T \quad 2\pi/3 \\
&\qquad (a/2 + \sqrt{3}l + \sqrt{3}f)/2 \quad (\sqrt{3}a/6 + l + f)/2 \quad 0]^T, \\
\mathbf{r}_3 &= [\mathbf{0}_2^T \quad -2\pi/3 \\
&\qquad -(a/2 + \sqrt{3}l + \sqrt{3}f)/2 \quad (\sqrt{3}a/6 + l + f)/2 \quad 0]^T,
\end{aligned}$$

and $\mathbf{r}_4 = \mathbf{0}_6$, where

$$f \equiv \frac{(b+c)(be^2 - 2d^3 + 3bd^2 + 6bde - 6de^2) - 2e^2c^2}{3(b+c)(e(b-c) + 2d(b-d))}.$$

The mass properties of the rigid links are computed from a CAD model, which yields

$$\begin{aligned}
m_1 &= m_2 = m_3 = 1.387 \times 10^{-3}\,\text{kg}, \\
m_4 &= 30.25 \times 10^{-3}\,\text{kg}, \\
[\mathbf{I}_1]_{\mathcal{R},1} &= [\mathbf{I}_2]_{\mathcal{R},2} = [\mathbf{I}_3]_{\mathcal{R},3}, \\
&= \text{diag}\,(0.1456 \quad 0.4656 \quad 0.5904) \times 10^{-9}\,\text{kg}\,\text{m}^2, \\
[\mathbf{I}_4]_{\mathcal{R},4} &= \text{diag}\,(12.63 \quad 12.63 \quad 252.1) \times 10^{-9}\,\text{kg}\,\text{m}^2.
\end{aligned}$$

The mass matrix is evaluated directly from these numerical values and the definition of eq. (7).

B. Potential Energy

Upon defining the lengths $g \equiv b/2 + L$ and $h \equiv \sqrt{3}a/6 + l + e$, screws $\mathbf{s}_i$, $i = 1, \ldots, m$, $m = 18$, are evaluated as

$$\begin{aligned}
\mathbf{s}_1 &= [0 \quad 0 \quad \pi \quad g - d - s_1 \quad -h - d \quad 0]^T, \\
\mathbf{s}_2 &= [0 \quad 0 \quad \pi \quad g - s_2 \quad -h \quad 0]^T, \\
\mathbf{s}_3 &= \left[0 \quad 0 \quad \pi/2 \quad c/2 \quad s_3 - \sqrt{3}a/6 - l \quad 0\right]^T \\
&= \mathbf{s}_9 = \mathbf{s}_{15}, \\
\mathbf{s}_4 &= \left[0 \quad 0 \quad \pi/2 \quad -c/2 \quad s_4 - \sqrt{3}a/6 - l \quad 0\right]^T \\
&= \mathbf{s}_{10} = \mathbf{s}_{16}, \\
\mathbf{s}_5 &= [0 \quad 0 \quad 0 \quad s_5 - g \quad -h \quad 0]^T, \\
\mathbf{s}_6 &= [0 \quad 0 \quad 0 \quad s_6 + d - g \quad -h - d \quad 0]^T, \\
\mathbf{s}_7 &= \Big[0 \quad 0 \quad -\pi/3 \quad \sqrt{3}(h+d)/2 - (g - d - s_7)/2 \\
&\qquad (h+d)/2 + \sqrt{3}(g - d - s_7)/2 \quad 0\Big]^T, \\
\mathbf{s}_8 &= \Big[0 \quad 0 \quad -\pi/3 \quad \sqrt{3}h/2 - (g - s_8)/2 \\
&\qquad h/2 + \sqrt{3}(g - s_8)/2 \quad 0\Big]^T, \\
\mathbf{s}_{11} &= \Big[0 \quad 0 \quad 2\pi/3 \quad \sqrt{3}h/2 + (g - s_{11})/2 \\
&\qquad h/2 - \sqrt{3}(g - s_{11})/2 \quad 0\Big]^T, \\
\mathbf{s}_{12} &= \Big[0 \quad 0 \quad 2\pi/3 \quad \sqrt{3}(h+d)/2 + (g - d - s_{12})/2 \\
&\qquad (h+d)/2 - \sqrt{3}(g - d - s_{12})/2 \quad 0\Big]^T, \\
\mathbf{s}_{13} &= \Big[0 \quad 0 \quad \pi/3 \quad -\sqrt{3}(h+d)/2 - (g - d - s_{13})/2 \\
&\qquad (h+d)/2 - \sqrt{3}(g - d - s_{13})/2 \quad 0\Big]^T, \\
\mathbf{s}_{14} &= \Big[0 \quad 0 \quad \pi/3 \quad -\sqrt{3}h/2 - (g - s_{14})/2
\end{aligned}$$

$$
\begin{aligned}
& h/2 - \sqrt{3}(g - s_{14})/2 \quad 0 \Big]^T, \\
\mathbf{s}_{17} \;=\; & \Big[0 \quad 0 \quad -2\pi/3 \quad -\sqrt{3}h/2 + (g - s_{17})/2 \\
& h/2 + \sqrt{3}(g - s_{17})/2 \quad 0 \Big]^T, \text{ and} \\
\mathbf{s}_{18} \;=\; & \Big[0 \quad 0 \quad -2\pi/3 \quad -\sqrt{3}(h+d)/2 + (g - d - s_{18})/2 \\
& (h+d)/2 + \sqrt{3}(g - d - s_{18})/2 \quad 0 \Big]^T.
\end{aligned}
$$

Turning our attention to the elastostatic properties of the compliant links, we realize that the beams are not all identical in that respect, since silicon crystal is an anisotropic material. The axes of the cubic crystal correspond to the axes of frame $\mathcal{F}$ shown in Fig. 8. As a result, the Young moduli E_i and the shear moduli G_i, $i = 1, \ldots, m$, are not all equal, depending on the orientation of their corresponding compliant link with respect to the crystal axes. Because of the symmetry in the crystal, we have

$$
\mathbf{H}_i = \operatorname{diag}\left(\frac{1}{G_\perp J}, \frac{1}{E_\perp I_Y}, \frac{1}{E_\perp I_Z}, \frac{1}{E_\perp A}, \frac{\alpha_Y}{G_\perp A}, \frac{\alpha_Z}{G_\perp A} \right), \tag{48}
$$

for $i = 1, \ldots, 6$, and

$$
\begin{aligned}
\mathbf{H}_i \;=\; \operatorname{diag}\Bigg(& \frac{1}{G_{\angle,T} J}, \frac{1}{E_\angle I_Y}, \frac{1}{E_\angle I_Z}, \\
& \frac{1}{E_\angle A}, \frac{\alpha_Y}{G_{\angle,Y} A}, \frac{\alpha_Z}{G_{\angle,Z} A} \Bigg),
\end{aligned} \tag{49}
$$

for $i = 7, \ldots, 18$, where the $\perp$ subscript refers to the beams that are at 0° or 90° from a crystal axis, and the $\angle$ subscript refers to the beams that are at 30° or 60° from a crystal axis. Because of material anisotropy, two distinct shear moduli are associated with the cross-sections that are not orthogonal to one of the crystallographic axes. These moduli, which we label $G_{\angle,Y}$ and $G_{\angle,Z}$, correspond, respectively, to the directions of the $Y_{\mathcal{S},i}$ and $Z_{\mathcal{S},i}$ axes of the cross-section frames $\mathcal{S}_i(s_i)$, $i = 7, \ldots, 18$. Moreover, in this model we neglect any coupling between torsion and bending due to the distinct shear moduli in compliant links $i = 7, \ldots, 18$. In fact, to avoid overcomplicating the problem, we define the section shear modulus in torsion as the average of the two actual shear moduli of the section, that is,

$$
G_{\angle,T} \equiv (G_{\angle,Y} + G_{\angle,Z})/2. \tag{50}
$$

This saves us from resorting to a modified Saint-Venant method, which would require the solution of a partial differential equation of the form

$$
G_{\angle,Y} \frac{\partial^2 \phi(y,z)}{\partial y^2} + G_{\angle,Z} \frac{\partial^2 \phi(y,z)}{\partial z^2} = 0, \tag{51}
$$

and where $\phi(y,z)$ represents the warping of the beam cross-sections. Hence, in the case of pure torsion, we consider the material to be isotropic with a shear modulus of $G_{\angle,T}$.

The numerical values of the foregoing elastic properties are given in Table V, as reported in [26]. The geometric properties of the beam cross-sections, also gathered in Table V, were computed from the formulae $J = \beta w t^3$, with $\beta = 0.258$, $I_Y = wt^3/12$, $I_Z = w^3 t/12$, and $A = wt$, whereas the shear correction factors are $\alpha_Y = \alpha_Z = 6/5$

TABLE V
CROSS-SECTION PROPERTIES OF THE COMPLIANT LINKS OF THE SBA

$E_\perp$	130.2 GPa	$G_\perp$	79.4 GPa
$E_{\angle,X}$	157.2 GPa	$G_{\angle,Y}$	79.4 GPa
$G_{\angle,Z}$	55.9 GPa	$G_{\angle,T}$	67.6 GPa
J	$0.8965 \times 10^{-16}\,\mathrm{m}^4$	I_Y	$0.2363 \times 10^{-15}\,\mathrm{m}^4$
I_Z	$0.2894 \times 10^{-16}\,\mathrm{m}^4$	A	$0.3150 \times 10^{-7}\,\mathrm{m}^2$
α_Y	1.2	α_Z	1.2

for rectangular cross-sections [27]. This permits the computation of the stiffness matrix as defined in eq. (28).

C. Dissipated Energy

It is assumed that all energy dissipation comes from air friction within the 2.5 μm gap between the proof mass and the handle wafer. Following the same method as in Section III, a Couette flow is assumed for in-wafer-plane proof-mass translations, while the air flow produced by proof-mass rotations and other rigid-link displacements are neglected. As in Section III, we may yet assume that an out-of-wafer-plane proof-mass translation generates a Poiseuille flow beneath it, but the triangular geometry of the proof mass prevents us from using the solution for rectangular plates. In order to obtain a rough estimate, let us assume a Poiseuille air flow beneath the proof mass that is orthogonal to the closest triangle edges, as sketched in Fig. 9. Consider now the small element of area underneath the proof mass that has a width dq and a total length of $a/\sqrt{3} - y$, where y is the coordinate of the element intersection with the Y-axis. We may assume that the damping due to this small element is given by the formula for rectangular plates that have one side much larger than the other [18], that is,

$$dc_Z = 96\eta(dq)(a/\sqrt{3} - y)^3/(\pi^4 p^3), \tag{52}$$

where $p = 2.5\ \mu$m is the gap between the proof mass and the handle wafer. Projecting the element width dq onto the Y-axis yields the relation $dq = \sqrt{3}dy/2$, which, upon substitution in eq. (52), allows for a summation over the upper branch of the triangular proof mass that leads to the integral

$$\begin{aligned} c_Z/3 &= \frac{48\sqrt{3}\eta}{\pi^4 p^3}\int_0^{a/\sqrt{3}} (a/\sqrt{3} - y)^3 dy \\ &= \frac{48\sqrt{3}\eta}{\pi^4 p^3}\int_0^{a/\sqrt{3}} y^3 dy \end{aligned}$$

whence,

$$c_Z = \frac{4\sqrt{3}\eta a^4}{\pi^4 p^3}, \tag{53}$$

thereby obtaining the result sought.

As a result, matrix $\mathbf{C}$ of eq. (30) takes the symbolic and numeric values

$$\mathbf{C} = \mathrm{diag}\left([\mathbf{0}_{21}^T \quad \eta A_4/p \quad \eta A_4/p \quad 4\sqrt{3}\eta a^4/(\pi^4 p^3)]^T\right), \text{ and}$$

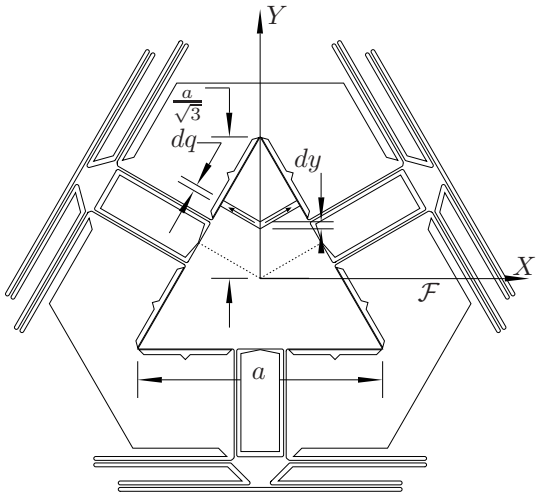

Fig. 9. Squeezed-film damping of the SBA proof mass

$$\mathbf{C} = \operatorname{diag}\left([\mathbf{0}_{21}^T \quad 3.12\times10^{-4} \quad 3.12\times10^{-4} \quad 8.19\times10^{2}]^T\right) \ \text{N·s/m}.$$

D. Estimated Dynamics

The first modes of the SBA are computed from eq. (35), which yields the results of Table VI. Because of the 24 degrees of freedom of the compliant mechanism, these results are somewhat more intricate. The first two frequencies differ only by round-off error, their associated modes involving motions of all four rigid links. For acceleration measurement, we are interested only in proof-mass motions, which are represented here by vector $\boldsymbol{\lambda}_{i,4}$. Apparently, from Table VI, the first two modes correspond to in-wafer-plane motions of the proof mass, with, in one case, a parasitic in-wafer-plane rotation. This parasitic motion is not due to round-off errors, but rather to silicon anisotropy. One must bear in mind, however, that the rotational component of $\boldsymbol{\lambda}_{i,4}$ is expressed in radians, whereas the translational component is expressed in meters. Hence, for instance, a $100\ \mu$m displacement of the proof mass along the direction of the first mode results in a parasitic rotation of 7.88 rad, or to relative position errors of the vertices of the proof mass of $0.788\ \mu$m. This result is thought to be acceptable; we may safely say that the fundamental frequency corresponds now to the two sensitive directions. In turn, the third natural frequency appears to be dominated by rotations, except for a small non-null value at the Z-axis translational direction of the proof-mass. In fact, mode $\boldsymbol{\lambda}_3$ may be visualized as a rotation of the proximal rigid links about their associated X_i axes—which are parallel to their corresponding edge of the triangular proof mass—and a translation—for the most part—of the proof mass along the Z-axis. Hence, we see that the natural frequency of the parasitic out-of-wafer-plane motion is now higher than that of the sensitive axes, which is, apparently, an advantage of the SBA mechanical architecture over that of the ADXL150 accelerometer.

TABLE VI

MODAL ANALYSIS OF THE SIMPLICIAL BIAXIAL ACCELEROMETER

i	1	2	3	4	5	6
f_i (Hz)	53.21	53.22	69.02	178.74	187.28	423.05
$\boldsymbol{\lambda}_{i,1}$	0.000	-0.000	-0.601	0.564	0.000	-0.998
	-0.000	0.000	0.000	0.000	0.058	0.000
	0.214	0.000	-0.000	-0.000	-0.000	-0.000
	-0.000	-0.000	-0.000	-0.000	-0.000	-0.000
	-0.000	0.486	0.000	-0.000	-0.000	-0.000
	0.000	-0.000	-0.000	0.001	0.000	0.003
$\boldsymbol{\lambda}_{i,2}$	-0.000	-0.000	-0.564	-0.311	-0.511	-0.028
	-0.000	0.000	-0.003	0.047	-0.027	-0.003
	-0.455	-0.452	-0.000	-0.000	-0.000	-0.000
	-0.000	0.000	0.000	-0.000	-0.000	0.000
	0.360	-0.243	-0.000	0.000	-0.000	-0.000
	-0.000	0.000	-0.000	-0.000	-0.001	0.000
$\boldsymbol{\lambda}_{i,3}$	0.000	-0.000	-0.564	-0.311	0.511	-0.028
	-0.000	0.000	0.003	-0.047	-0.027	0.003
	-0.455	0.452	-0.000	-0.000	-0.000	-0.000
	-0.000	-0.000	-0.000	-0.000	0.000	0.000
	-0.360	-0.243	-0.000	0.000	0.000	-0.000
	0.000	-0.000	-0.000	-0.000	0.001	0.000
$\boldsymbol{\lambda}_{i,4}$	-0.000	-0.000	-0.040	0.695	0.000	-0.050
	-0.000	-0.000	0.000	-0.000	-0.688	-0.000
	0.328	0.000	-0.000	-0.000	0.000	-0.000
	0.416	0.000	0.000	0.000	-0.000	0.000
	0.000	-0.486	-0.000	0.000	0.000	0.000
	-0.000	0.000	0.003	0.000	0.000	0.000

In order to evaluate the effect of damping over the accelerometer, matrix $\mathbf{H}(s)$ is computed according to eq. (36). As in Section III, we apply d'Alembert's principle of inertia forces to the dynamic system, taking the inertia forces acting on the rigid links as input forces of eq. (33), the outputs being the proof mass displacements. In particular, upon applying successively pure accelerations along the X, Y, and Z-axis directions, we obtain the complex frequency responses $h_X(\omega)$, $h_Y(\omega)$, and $h_Z(\omega)$, respectively, of translations of the proof mass in each of these directions. The magnitudes and phase angles of these frequency responses are shown in the Bode plots of Fig. 10. The lower sensitivity of the proof-mass displacements to Z-axis accelerations than to the X- and Y-axis accelerations is confirmed from Fig. 10(a). One may also observe a good isotropy for in-wafer-plane accelerations, and a bandwidth of approximately 100 rad/s.

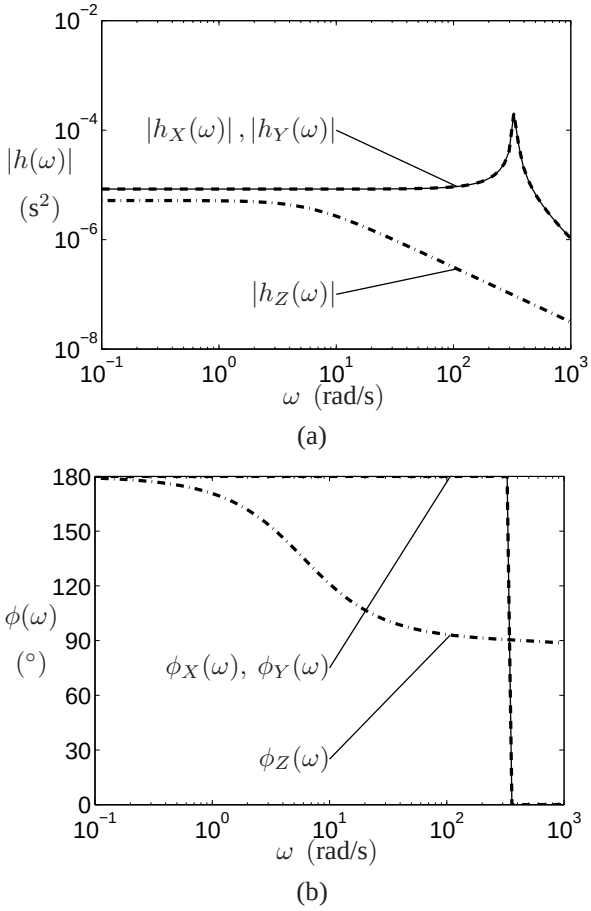

Fig. 10. Frequency response of the SBA: (a) magnitude and (b) phase angle

E. Measured Dynamics

The mechanical structure of the SBA was tested by applying to it short impulse accelerations in the negative direction of its Z axis, as defined in Fig. 8. The "free" resonations of the structure were then recorded using a vibrometer. A schematic and a picture of the test bench are shown in Fig. 11. In this setup, the shaker (Brüel & Kjær Mini-Shaker 4810) is driven by a regular sound amplifier (Harman Kardon HK3300), which itself takes its input from a signal generator. A typical time-history of the shaker impulse input voltage is displayed in Fig. 12. The resulting motions of the SBA rigid-links are recorded by the vibrometer (Polytec PSV-400), which sheds a laser beam vertically down on the sample. The laser beam is programmed to scan 382 points on the SBA, according to the mesh shown in Fig. 13. Point-velocities are measured by the vibrometer, and, thence, a frequency-domain distribution of the point-velocities of the accelerometer architecture is computed and recorded by the controller (Polytec OFV–5000).

The Polytec controller returns a frequency-domain distribution of the velocities of the scanned points $\{S_j\}_{j=1}^{382}$, along with their phase correspondance with a reference signal. As can be seen from Fig. 11(a), in the test bench, the

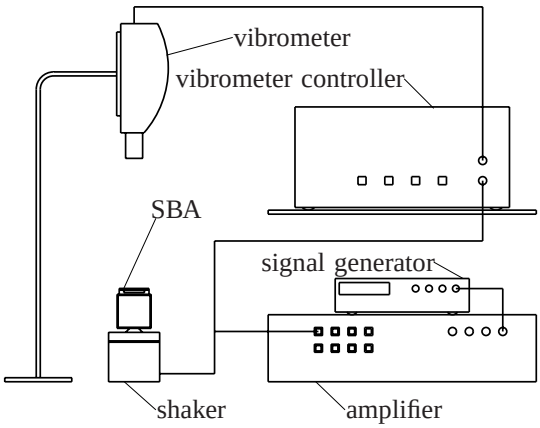

(a)

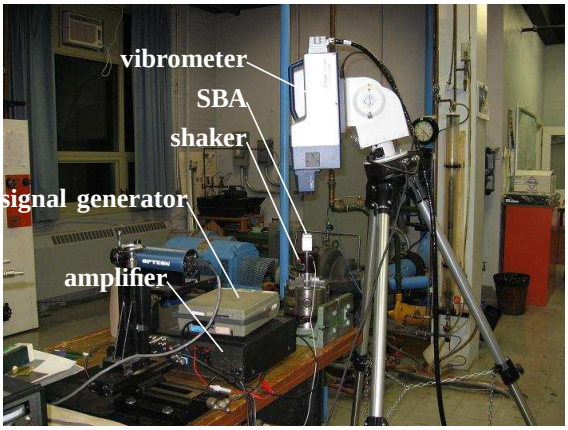

(b)

Fig. 11. SBA test bench: (a) schematic representation and (b) photograph

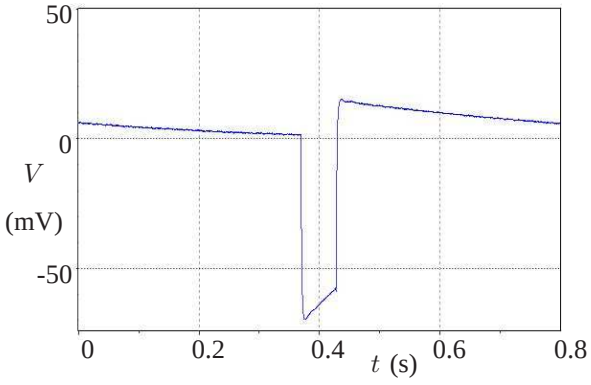

Fig. 12. Typical voltage impulse applied at the shaker input

shaker input voltage was used as the reference signal. From these results, the complex velocity frequency response $v_j(\omega)$ of each point may be computed.

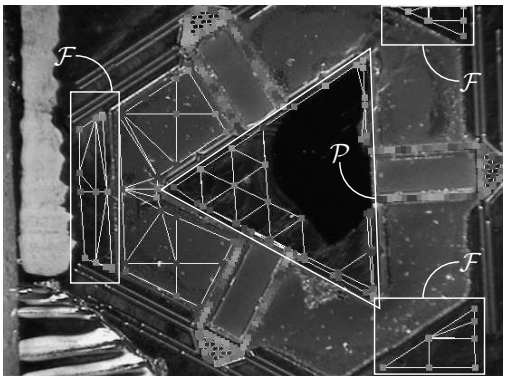

Fig. 13. Points scanned by the vibrometer

The point-displacement frequency response $d_j(\omega)$ may then be obtained as

$$d_j(\omega) = v_j/(\omega i), \tag{54}$$

where $i \equiv \sqrt{-1}$. On the other hand, point-acceleration frequency response $a_j(\omega)$ is given by

$$a_j(\omega) = \omega i v_j. \tag{55}$$

Let us now define the sets $\mathcal{F}$ and $\mathcal{P}$ of the indices of the points pertaining to the accelerometer frame and proof mass, respectively, **as illustrated on Fig. 13.** From this, we may reference the proof-mass point-displacement response magnitudes with the rms-value of the frame point-acceleration response magnitudes. This yields the normalized displacements

$$\bar{d}_j(\omega) = \frac{d_j(\omega)}{\sqrt{\frac{1}{n}\sum_{k\in\mathcal{F}} |a_k(\omega)|^2}}, \quad j \in \mathcal{P}, \tag{56}$$

where n is the cardinality of $\mathcal{F}$. Finally, we obtain an overall magnitude response of the proof mass by taking the rms-value of the displacements of its 60 scanned points. Symbolically, we have

$$\bar{d}_{rms}(\omega) = \sqrt{\frac{1}{m}\sum_{j\in\mathcal{P}} |\bar{d}_j(\omega)|^2}, \tag{57}$$

where $m = 60$ is the cardinality of $\mathcal{P}$. On the other, the meaning of an overall phase diagram of the proof-mass point-displacements is less apparent, and, therefore, it was decided to leave them separate. Hence, the phase angle $\bar{\phi}_j(\omega)$ of point $j \in \mathcal{P}$ is readily computed as

$$\bar{\phi}_j = \arctan\left[\frac{\Im\{\bar{d}_j(\omega)\}}{\Re\{\bar{d}_j(\omega)\}}\right]. \tag{58}$$

The resulting frequency response is shown in Figs. 14(a) and (b), along with the modeled frequency response, which was already shown in Fig. 10. Notice that the 60 phase angles $\bar{\phi}_j$, $j \in \mathcal{P}$ are displayed in Fig. 14(b). As can be seen from these figures, the measured frequency response is fairly close to the ones given by the transfer functions $h_X(\omega)$ and $h_Y(\omega)$. The modeled and measured peak frequencies are 53.2 Hz and 46.3 Hz, respectively.

This difference may be due in part to the rough approximation of the damping coefficient, which appears to have been underestimated.

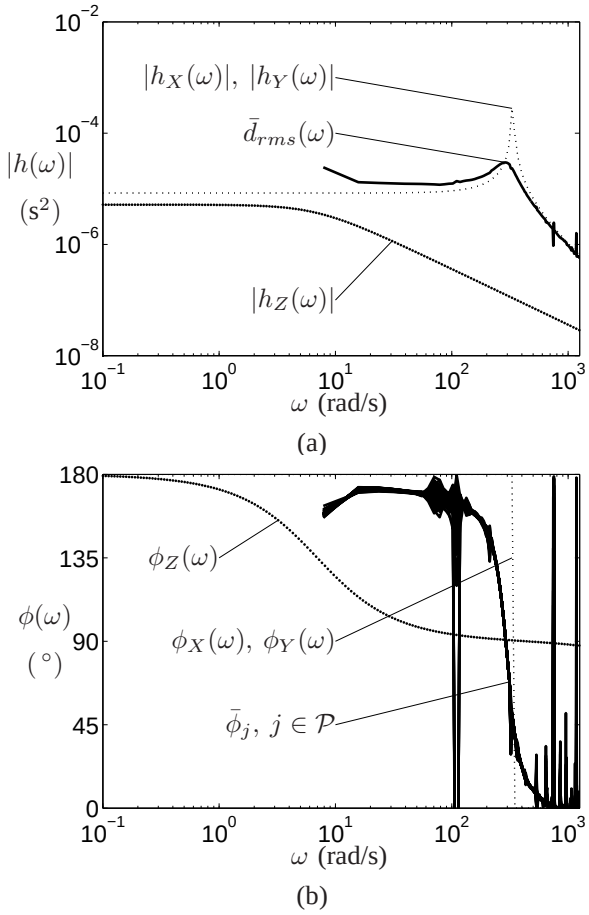

Fig. 14. Comparison between the SBA model and the experimental results: (a) magnitudes and (b) phase angles

V. CONCLUSIONS

Although the assumptions put forward in this article are common in elastodynamics modeling, the mathematical tools used are not. In particular, screw theory allows for a sound, broad-scope, and simple formulation of the dynamic model of a lumped MEMS. The general framework in which the proposed method is developed is important for the evaluation of large numbers of variants with different topologies, numbers of degrees of freedom, etc. Moreover, the simplicity of the resulting model formulation is thought to be of crucial importance, since the usefulness of a symbolic solution is generally dictated by its level of intricacy. A major factor contributing to the simplicity of the dynamic model obtained is the parameters chosen for the representation of rigid-link rotations in space. As shown in eq. (5), for small displacements, the time rates of these parameters are approximately equal to the rigid-link angular velocity, which simplifies the model

formulation. The resulting symbolic models should yield information on the relations between the design parameters and the design objectives. This is thought to be especially important in MEMS design, e.g., for assessing the scalability of a design, the effect of constraints on certain dimensions due to microfabrication limitations, the overall feasibility of certain actuation schemes, estimating parasitic displacements, etc.

The model was applied to the relatively simple mechanical architecture of the adready-existing ADXL150 accelerometer, and the estimated dynamic properties of the device were compared to published data, which confirmed the accuracy of the proposed model. The dynamic model was then applied to the SBA, an accelerometer that comprises four rigid links and 18 compliant links. The modeled and measured dynamic properties of the mechanism were compared, which corroborated the previous results. Furthermore, the two case studies showed that the proposed formulation can streamline both symbolic and numeric calculations when the complete system dynamics is to be modeled.

An example of a potential application of this method to MEMS synthesis comes from the expression of the stiffness matrix obtained in eq. (28), which is completely decoupled. Indeed, $\mathbf{K}$ appears as a product of matrices $\mathbf{R}$, $\mathbf{A}$, and $\mathbf{B}$, containing the information on the rigid-link poses, the mechanism topology, and the compliant-link stiffness properties, respectively. This should prove useful for the synthesis of lumped-compliance micromechanisms. **As an example, one could impose the rigid-link poses and the compliant links used for a particular MEMS, and then treat the topology $\mathbf{A}$ as a design variable**. Another potential application of this method could come from its combination with the model proposed in [28]. In this reference, the authors modeled the dynamics of a compliant micromechanism subjected to nonlinear external forces by approximating its displacements with a time-varying linear combination of its modes. These modes are computed from a linear dynamic model similar to that of eq. (33), except that the compliant links are discretized rather than treated as continua. Treating the compliant links as Euler-Bernoulli beams—or any other compliance model—and expressing the system state in terms of rigid-link poses, twists, and twist-rates minimizes the number of generalized coordinates of the associated model. Since computing the stiffness matrices of Euler-Bernoulli beams is a linear process, and because the dimension of the associated nonlinear eigenvalue problem is minimized, this method should streamline the computation of the mechanism dynamic response.

VI. Acknowledgments

The support of both NSERC, through a Canada Graduate Scholarship awarded to the first author, and FQRNT, through Research Grant PR-112531, are dutifully acknowledged. The assistance of the McGill Microfabrication Laboratory (funded by CFI, NSERC and VRQ) in preparing prototypes of the Simplicial Biaxial Accelerometer analyzed in section IV is also acknowledged.

REFERENCES

[1] H. Qu, D. Fang, and H. Xie, "A monolithic cmos-mems 3-axis accelerometer with a low-noise, low-power dual chopper amplifier," in *Solid-state Sensors, Actuators and Microsystem Workshop*, Hilton Head, June 2006, pp. 224–227.

[2] K. A. Jensen, C. P. Lusk, and L. L. Howell, "An xyz micromanipulator with three translational degrees of freedom," *Robotica*, vol. 24, no. 3, pp. 305–314, 2006.

[3] S. D. Senturia, N. Aluru, and J. White, "Simulating the behavior of MEMS devices: Computational methods and needs," *IEEE Computational Science & Engineering*, vol. 4, no. 1, pp. 30–43, 1997.

[4] K.-J. Bathe, *Finite Element Procedures in Engineering Analysis*. Englewood Cliffs, NJ, USA: Prentice-Hall, 1982.

[5] B. D. Jensen, M. P. de Boer, N. D. Masters, F. Bitsie, and D. A. L. Van, "Interferometry of actuated microcantilevers to determine material properties and test structure nonidealities in MEMS," *IEEE Journal of Microelectromechanical Systems*, vol. 10, no. 3, pp. 336–346, 2001.

[6] S. K. De and N. R. Aluru, "Lagrangian scheme for dynamic analysis of electrostatic MEMS," *IEEE Journal of Microelectromechanical Systems*, vol. 13, no. 5, pp. 737–758, 2004.

[7] E. Wittbrodt, I. Adamiec-Wójcik, and S. Wojciech, *Dynamics of Flexible Multibody Systems*, ser. Foundations of Engineering Mechanics. Springer Berlin Heidelberg, 2006.

[8] U. Kirsch, "Optimal topologies of structures," *Applied Mechanics Reviews*, vol. 42, no. 8, pp. 223–239, 1989.

[9] K.-J. Lu and S. Kota, "Topology and dimensional synthesis of compliant mechanisms using discrete optimization," *ASME Journal of Mechanical Design*, vol. 128, pp. 1080–1091, 2006.

[10] S. Nishiwaki, M. I. Frecker, S. Min, and N. Kikuchi, "Topology optimization of compliant mechanisms using the homogenization method," *International Journal for Numerical Methods in Engineering*, vol. 42, no. 3, 1998.

[11] L. L. Howell, *Compliant Mechanisms*. New York, NY, USA: John Wiley & Sons, 2001.

[12] S. M. Lyon, P. A. Erickson, M. S. Evans, and L. L. Howell, "Prediction of the first modal frequency of compliant mechanisms using the pseudo-rigid-body model," *ASME Journal of Mechanical Design*, vol. 121, no. 2, pp. 309–313, 1999.

[13] Y.-Q. Yu, L. L. Howell, C. Lusk, Y. Yue, and M.-G. Hen, "Dynamic modeling of compliant mechanisms based on the pseudo-rigid-body model," *ASME Journal of Mechanical Design*, vol. 127, pp. 760–765, 2005.

[14] L. Meirovitch, *Analytical Methods in Vibrations*. New York, NY, USA: Macmillan Publishing Co., 1967.

[15] J. M. Selig and X. Ding, "A screw theory of static beams," in *Proceedings of the 2001 IEEE/RSJ International Conference on Intelligent Robots and Systems*, Maui, Hawaii, USA, 2001, pp. 312–317.

[16] A. A. Shabana, "Flexible multibody dynamics: Review of past and recent developments," *Multibody System Dynamics*, vol. 1, no. 2, pp. 189–222, 1997.

[17] P. Stellman, T. Buchner, W. J. Arora, and G. Barbastathis, "Dynamics of nanostructured origami," *IEEE Journal of Microelectromechanical Systems*, vol. 16, no. 4, pp. 932–949, 2007.

[18] S. Senturia, *Microsystem Design*. Boston, USA: Kluwer Academic Publishers, 2001.

[19] J. Angeles, *Fundamentals of Robotic Mechanical Systems*, 3rd ed. New York: Springer, 2007.

[20] R. J. Roark and W. C. Young, *Formulas for Stress and Strain*, 5th ed. McGraw-Hill, 1975.

[21] J. M. Selig, *Geometrical Methods in Robotics*, ser. Monographs in Computer Science. Springer, 1996.

[22] J. Angeles, K. E. Zanganeh, and S. Ostrovskaya, "The analysis of arbitrarily-damped linear mechanical systems," *Archive of Applied Mechanics*, vol. 69, pp. 529–541, 1999.

[23] B. R. Munson, D. F. Young, and T. H. Okiishi, *Fundamentals of Fluid Mechanics*, 5th ed. Hoboken, NJ, USA: J. Wiley & Sons, 2006.

[24] P. Cardou and J. Angeles, "Simplectic architectures for true multi-axial accelerometers: A novel application of parallel robots," in *IEEE International Conference on Robotics and Automation*, Rome, Italy, April 2007, pp. 181–186.

[25] M. L. Culpepper and G. Anderson, "Design of a low-cost nano-manipulator which utilizes a monolithic, spatial compliant mechanism," *Precision Engineering*, vol. 28, pp. 469–482, 2004.

[26] J. J. Wortman and R. A. Evans, "Young's modulus, shear modulus, and Poisson's ratio in silicon and germanium," *Journal of Applied Physics*, vol. 36, no. 1, pp. 153–156, 1965.

[27] W. D. Pilkey, *Formulas for Stress, Strain, and Structural Matrices*, 2nd ed. John Wiley & Sons, 2005.

[28] G. K. Ananthasuresh, R. K. Gupta, and S. D. Senturia, "Approach to macromodeling of MEMS for nonlinear dynamic simulation," in *DSC*, vol. 59, ASME. Dynamic Systems and Control Division, 1996, pp. 401–407.